

Semitransparent Layers of Social Self-Sorting Merocyanine Dyes for Ultranarrow Bandwidth Organic Photodiodes

Tim Schembri, Jin Hong Kim, Andreas Liess, Vladimir Stepanenko, Matthias Stolte, and Frank Würthner*

Two dipolar merocyanines consisting of the same π -conjugated chromophore but different alkyl substituents adopt very different packing arrangements in their respective solid state with either H- or J-type exciton coupling, leading to ultranarrow absorption bands at 477 and 750 nm, respectively, due to exchange narrowing. The social self-sorting behavior of these push-pull chromophores in their mixed thin films is evaluated and the impact on morphology as well as opto-electronical properties is determined. The implementation of this well-tuned two-component material with tailored optical features allows to optimize planar heterojunction organic photodiodes with fullerene (C₆₀) with either dual or single wavelength selectivity in the blue and NIR spectral range with ultranarrow bandwidths of only 11 nm (200 cm⁻¹) and an external quantum efficiency of up to 18% at 754 nm under 0 V bias. The application of these photodiodes as low-power consuming heart rate monitors is demonstrated by a reflectance-mode photoplethysmography (PPG) sensor.

on organic semiconductors made significant progress in devices like organic light emitting diodes,^[11] organic thin-film transistors (OTFTs),^[12] and organic solar cells (OSCs).^[13] This progress can be ascribed to the better tunability of material properties,^[12] allowing for customized optical properties including sufficient semitransparency, but also to their inherent tinctorial strength enabling light-weight devices on flexible substrates.^[14–16] Whilst panchromatic light harvesting is desired for OSCs, a particularly advantageous application of organic semiconductors are color-selective organic photodiodes (OPDs)^[17–19] which can be realized based on rational molecular design,^[20] on exciton coupling and exchange narrowing of chromophores in the solid state (J-/H-aggregates)^[21,22] and on smart device engineering approaches like

charge collection narrowing^[23–25] or by micro-cavity design.^[26,27] Still the major challenge is to balance the efficiency of these detectors with their respective sensitivity toward high-performance color selective OPDs for, that is, biomedical monitoring and sensing applications with low power consumption.^[28] Especial interest herein lies on image sensors of multiple stacked semitransparent OPDs as opposed to a typical color filter array on panchromatic photodiodes with which different wavelengths are detected spatially separated from each other.^[29] This allows for an increase in the geometric fill factor of such sensors, ultimately increasing the maximum resolution of an OPD.^[18]

Herein we make use of the social self-sorting behavior of a mixture of two dipolar merocyanine dyes, 1(Pyrl) and 1(Hex), upon thin-film formation by a simple spin coating and thermal annealing procedure to accomplish highly transparent OPDs (visible light transmission $T\lambda \approx 70\text{--}80\%$). These two merocyanines self-assemble exclusively into H- (1(Pyrl); 477 nm) and J-type (1(Hex); 750 nm) coupled aggregates in their respective neat layers. The social incorporation of one push-pull chromophore into the aggregate structure of the other not only has an impact on the narrow absorption bands but also on the morphology of the mixed thin film, impacting the charge transport behavior as well as the performance of the respective ultranarrow bandwidth OPDs in a planar heterojunction (PHJ) device architecture with fullerene C₆₀. Single and dual wavelength selective devices could be designed with external quantum efficiencies (EQE) of up to 18% with responsivities (R) of 109 mA W⁻¹ and full-width at half maximum (FWHM) values of down to 11 nm (200 cm⁻¹), which were demonstrated in a reflectance-mode photoplethysmography (PPG) application.

1. Introduction

Semitransparent opto-electronic materials are key elements for energy harvesting devices and a large variety of sensor applications.^[1–4] Such materials require a precise control of their optical properties not only for aesthetic reasons but also for improving their functions, such as for the use of greenhouse integrated semitransparent solar cells^[5] or infrared regulating smart windows.^[6] While today's state of the art opto-electronic applications are still majorly based on inorganic semiconductors like doped silicon, gallium,^[7,8] or hybrid perovskite materials,^[9,10] in the last decades new emerging technologies based

T. Schembri, Dr. J. H. Kim, Dr. A. Liess, Dr. M. Stolte, Prof. F. Würthner
Universität Würzburg


Center for Nanosystems Chemistry (CNC)
and Bavarian Polymer Institute (BPI)

Theodor-Boveri-Weg, Würzburg 97074, Germany
E-mail: wuerthner@uni-wuerzburg.de

Dr. V. Stepanenko, Dr. M. Stolte, Prof. F. Würthner
Universität Würzburg

Institut für Organische Chemie

Am Hubland, Würzburg 97074, Germany

 The ORCID identification number(s) for the author(s) of this article can be found under <https://doi.org/10.1002/adom.202100213>.

© 2021 The Authors. Advanced Optical Materials published by Wiley-VCH GmbH. This is an open access article under the terms of the Creative Commons Attribution License, which permits use, distribution and reproduction in any medium, provided the original work is properly cited.

DOI: 10.1002/adom.202100213

2. Results and Discussion

2.1. Absorption Properties of Thin Films

Both push-pull dyes **1(Pyrl)** and **1(Hex)** are composed of the same 2-[4-(*tert*-butyl)thiazol-2(3H)-ylidene]malononitrile acceptor (A) and a 2-aminothiophene donor (D) unit and vary only in their alkyl substituents. Merocyanine dye **1(Hex)** inherits two long aliphatic hexyl chains, while **1(Pyrl)** has a rigid and more compact pyrrolidino group as donor moiety (see **Figure 1a**). Synthesis was performed according to literature-known procedures^[22,30] and as both chromophores share the same π -scaffold, their molecular properties are almost identical. Accordingly, in solution both dyes show a very similar narrow and intense charge-transfer absorption band at 651–652 nm (Figure 1b, $\epsilon_{\max} \approx 124\,000\text{ M}^{-1}\text{ cm}^{-1}$ in CH_2Cl_2), have a ground state dipole moment of 13–14 D and a first oxidation potential of 0.34–0.37 V, which render them suitable candidates as electron donating materials in organic opto-electronic applications.^[22,31] Most remarkably, upon solution processing into thin films via spin coating and additional thermal annealing, their optical signatures are significantly altered due to the impact of the different donor substituents on the molecular packing arrangement in the solid state (Figure 1b). The compact pyrrolidino group guides **1(Pyrl)** into a card-stack like arrangement of anti-parallelly aligned chromophores with prominent H-type coupling and a narrow hypsochromically shifted absorption band at 479 nm with a *FWHM* of 17 nm (740 cm^{-1}). For **1(Hex)** the long and flexible hexyl groups induce a head-to-tail arrangement with predominant J-type coupling, as proven for similar chromophores, inducing a significantly bathochromically shifted absorption band to 750 nm with a *FWHM* of 19 nm (340 cm^{-1}).^[22,30] While a zig-zag arrangement, that is, non-ideal J-type packing arrangement with an additional weak H-band, was found for the related **1(Pr)**^[30] derivative, a sharper and more distinct J-band (and lack of an H-band) is observed for **1(Hex)**.

Intrigued by these two distinct blue- and NIR-wavelength selective optical signatures of two molecularly such similar dyes, we were motivated to elucidate the impact of molecular interactions in mixed thin-films on optical properties and device performances. As the absorption spectra of crystalline domains of **1(Pyrl)** and **1(Hex)** in their thin films each only exhibit one prominent and very narrow absorption feature at either 477 or 750 nm, respectively, the amount of dyes in each molecular packing arrangement in mixed thin films can be deduced by the relative intensity of these two absorption bands. Hence, thin films were deposited onto quartz substrates at 3000 rpm from mixtures of **1(Pyrl)**:**1(Hex)** in CHCl_3 solution ($c_{\text{total}} = 4 \times 10^{-3}\text{ M}$) and afterward annealed at 130 °C for 5 min (Figure 1b). As the two selected dyes show different solubilities, it was verified by NMR experiments, that the mixing ratio of the solution was retained after thin film deposition (see Figure S1, Supporting Information). Additionally, thin films were cast from solutions with varying concentrations of each individual dye to prove that the concentration does not affect the formation and the respective absorption profiles of the aggregates and a linear correlation between absorbance and concentration is given (Figure S2, Supporting Information).

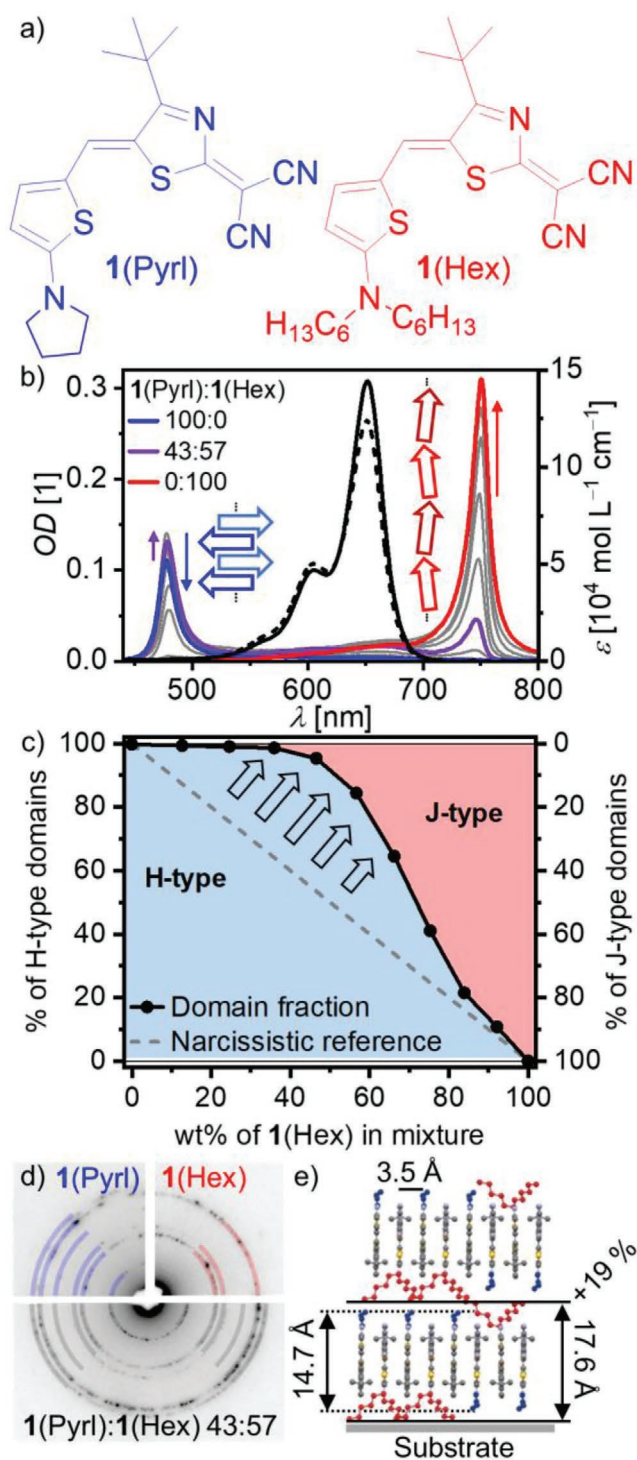


Figure 1. a) Chemical structures of the investigated merocyanine dyes **1(Pyrl)** and **1(Hex)**. b) UV-vis-NIR absorption spectra of mixed **1(Pyrl)**:**1(Hex)** thin films at weight ratios ranging from 100:0 (blue) over 43:57 (violet; equals a 50:50 molar ratio) to 0:100 (red) spin coated from a CHCl_3 solution ($c_{\text{total}} = 4 \times 10^{-3}\text{ M}$) onto quartz substrates after annealing at 130 °C for 5 min; the monomer extinction spectra in CHCl_3 of **1(Pyrl)** (black dashed) and **1(Hex)** (black solid) are provided as reference; the insets show schematics of the respective packing arrangements in pure thin films with molecules simplified as ground state dipole moments. c) Calculated fractions of H- and J-type domains in mixed thin films in

In order to quantitatively correlate the 1(Pyrl):1(Hex) mixing ratio to the predominant exciton coupled domain at a given ratio, optical properties of mixed thin films at different mixing conditions were investigated. While the optical densities (*ODs*) of annealed neat thin films of 1(Pyrl) and 1(Hex) of equal thickness of about 10 ± 3 nm on quartz are 0.11 and 0.31 (Figure 1b; Figure S3, Supporting Information), respectively, the before mentioned linear behavior of $OD(c_{total})$ is not retained for mixed layers. Exemplarily, the absorption spectrum of a thin film cast from a mixture with a 43:57 weight fraction of 1(Pyrl):1(Hex) (50:50 molar ratio) is highlighted in Figure 1b together with the absorption of the individual dyes and thin films at intermediate mixing ratios. It is evident, that while the J-band of 1(Hex) at this mixing ratio is strongly decreased to an *OD* of only 0.05 (16%) and slightly blue shifted by 4 nm to 746 nm, the H-band is significantly enhanced up to 0.13 (118%) and exhibits a red shift of 1 nm to 478 nm compared to the absorption of a neat 1(Pyrl) layer. From the absorption values of the mixed thin films for the H- and the J-band of various mixing ratios along with further optical characterization techniques to ensure data homogeneity and comparability (Table S1, Figures S3–S5, Supporting Information), the fraction of H- and J-type domains within the thin films can be deduced (see Supporting Information for details on the calculation) and the results are given in Figure 1c. Here it becomes evident that between fractions of 100:0 and 64:36 H-type coupled domains prevail almost exclusively in the mixed thin films. Hence, no domains with J-type coupled chromophores can be detected, meaning that solely domains with H-coupled chromophores are formed despite the presence of 1(Hex) in the thin film. An enhanced intensity of the H-band is observed up to a ratio of 84% 1(Hex) and only for larger amounts of 1(Hex) the ratio of H- and J-type domains follows an ideal narcissistic behavior (i.e., phase separation) in which both dyes self-assemble into separated domains.

2.2. Electron and X-Ray Diffraction of Thin Films

The observed self-sorting^[32] behavior of these dyes in thin films is indeed quite impressive compared to observations made previously for self-assembled dye aggregates in solution.^[33] To investigate if this preference for social self-sorting (i.e., mixing) into domains with H-type coupling can be ascribed to the formation of co-crystallites composed of 1(Pyrl) and 1(Hex), selected area electron diffraction (SAED) and X-ray diffraction (XRD) measurements of thin films of the single components as well as for a 43:57 mixture (50:50 molar ratio) were performed.

dependence on the weight fraction of 1(Hex) in the solution used for preparation; the solid line serves as guide to the eye for the social self-sorting and the dashed line corresponds to the values expected for a complete narcissistic behavior. d) SAED patterns of polycrystalline regions of annealed thin films of 1(Pyrl), 1(Hex) as well as a 43:57 mixture thereof. The blue and red circle fragments indicate the position of the diffraction cycles arising due to the packing of 1(Pyrl) leading to H-coupling and of 1(Hex) to J-coupling, respectively. e) Proposed packing of a mixed thin film of 1(Pyrl) and 1(Hex) on the substrate with indicated layer distances of the π - π -stacking (top) as well as the layer stacking parallel to the substrate (left: distance in pure thin films of 1(Pyrl); right: distance in mixed thin films of 1(Pyrl) and 1(Hex)).

SAED measurements (Figure S6, Table S2, Supporting Information) give information about interplanar distances of planes oriented perpendicular to the substrate and the diffraction patterns are shown in Figure 1d. Here for a thin film of 1(Pyrl) six diffraction cycles are clearly observed, corresponding to *d*-spacing values of 9.8, 5.6, 5.0, 4.0, 3.4, and 3.2 Å. In contrast, the thin film of 1(Hex) shows only 3 diffraction cycles which yield *d*-spacing values of 5.8, 5.1, and 3.5 Å. The diffraction pattern of the thin film of a 43:57 mixture again shows 6 diffraction cycles with *d*-spacings of 10.0, 5.6, 5.0, 4.0, 3.5, and 3.2 Å, with the similar number and *d*-spacing of these 6 diffraction cycles indicating that the 43:57 mixed thin film predominantly adopts a similar in-plane molecular packing structure as neat 1(Pyrl). By powder XRD measurements (Figure S7, Supporting Information), which give complementary information about the planes oriented parallel to the substrate, distinct reflexes are observed at $2\theta = 6.0^\circ$ for thin films of 1(Pyrl) and at $2\theta = 4.1^\circ$ for thin films of 1(Hex), corresponding to *d*-spacings of 14.7 and 21.5 Å, respectively. For the thin film of the 43:57 mixture, only one slightly broadened reflex is observed at $2\theta = 5.7^\circ$, yielding an interplanar distance of 17.6 Å.

Therefore, the diffraction results demonstrate that the 43:57 mixed thin film follows the in-plane packing arrangement of 1(Pyrl) (SAED results) but with 19% increased out-of-plane distances (XRD results). Based on the above analyses, the packing structure of the mixed thin film is proposed as shown in Figure 1e. Thus, up to 40% of the molecules of 1(Hex) can be socially incorporated in the card stack like packing arrangement of 1(Pyrl) as they have equal dipole moments and the chromophore backbone shape is identical. Up to a mixing ratio of 43:57 the formation of two-component domains also increases the total absorbance of H-type domains by up to 20%. However, the larger substituents of 1(Hex) also account for the larger interplanar distance perpendicular to the substrate observed in XRD measurements (17.6 Å vs 14.7 Å). On the other hand, molecules of 1(Pyrl) are not incorporated into the zig-zag structure of 1(Hex) due to their compact donor substituents, which strongly favors a card stack like packing with a low longitudinal shift. Due to the lower sterical demand, a social self-sorting behavior is observed for mixtures up to mixing ratios of 16:84 1(Pyrl):1(Hex), but a narcissistic self-sorting for an excess of 1(Hex). These results demonstrate that the H-type packing with antiparallel alignment of the dipolar dyes is the preferred arrangement for this chromophore in the absence of bulky sidechains. The fact that up to a molar ratio of 50:50 a cofacial stacking in H-type coupled domains prevails further suggests that the dyes 1(Pyrl) and 1(Hex) are packed in an alternating fashion in the π -stacks, thereby providing sufficient space for the hexyl chains between the respective layers (Figure 1e).

2.3. Planar-Heterojunction Organic Photodiodes

Based on the interesting optical properties of 1(Pyrl):1(Hex) mixed thin films, we investigated PHJ OPDs at different mixing ratios thereof to elucidate the impact of this multi-component electron donor material on device performance. The OPDs were fabricated on glass/indium tin oxide(ITO)/molybdenum oxide(MoO₃) substrates from mixed solutions as

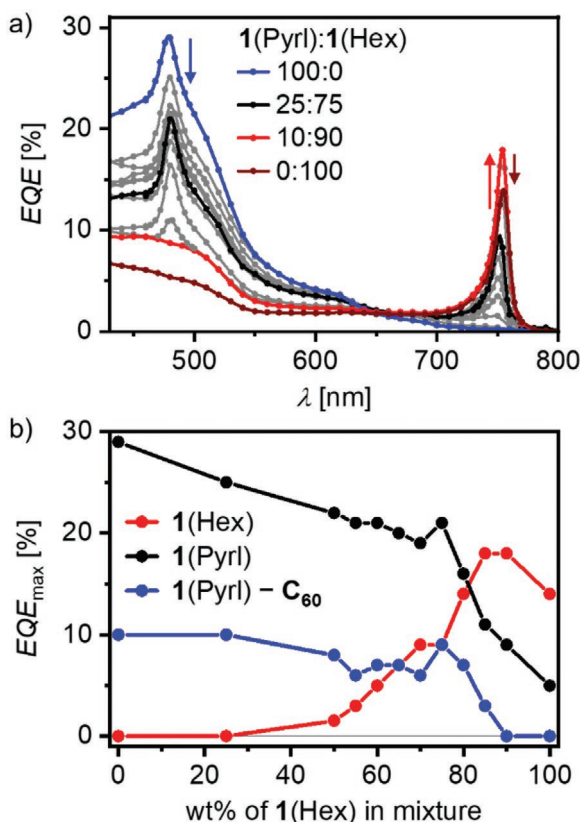


Figure 2. a) EQE spectra of PHJ OPDs in an ITO/MoO₃/1(Pyrl):1(Hex)/30 nm C₆₀/BCP/Ag architecture with a spin coated mixed 1(Pyrl):1(Hex) donor layer at different mixing ratios ranging from 100:0 (blue) over 25:75 (black) and 10:90 (red) to 0:100 (brown). b) EQE_{max} values in dependence on the weight fraction of 1(Hex) in the mixture at λ_{max} of 1(Hex) (red, 754 nm), 1(Pyrl) (blue, 480 nm), and 1(Pyrl) with correction for parasitic C₆₀ absorption (black); the solid lines serve as guide to the eye.

described above. Compared to our previously reported results on OPDs of 1(Pyrl),^[22] here an optimized device architecture

consisting of an ITO/6 nm MoO₃/donor/30 nm C₆₀/5 nm BCP/100 nm Ag PHJ stack was established, which benefits from the selective electron and hole transporting layers to yield higher reproducibility along with improved device stability (vide infra). The optimal merocyanine layer thickness was determined to be < 8 nm, which could be obtained from spin coating a solution with 1.5 mg mL⁻¹ of 1(Hex). Accordingly, all mixed layers were deposited at equal concentration while varying the weight fraction of 1(Pyrl) and 1(Hex)

As shown in **Figure 2**, OPD devices at all mixing ratios with both single and dual wavelength selectivity could be realized. As expected, the changes in optical absorption profiles correspond well to prior thin-film investigations (vides supra, Figure S8a, Supporting Information). Only an additional contribution in the spectral range below 550 nm can be ascribed to the absorbance of the 30 nm thick C₆₀ acceptor layer. With variation of the 1(Pyrl):1(Hex) mixing ratio from 100:0 to 0:100 wt%, a successive step-wise evolution of the current-density, and voltage (J - V) characteristics from the pristine H- to the pristine J-type characteristics of 1(Pyrl) to 1(Hex), respectively, is observed (for details see Figure S8b, Table S3, Supporting Information). The corresponding EQE spectra (Figure 2a) reveal the spectral features of the combined mixed donor and acceptor layers. Unfortunately, the maximum EQE (EQE_{max}) at the H-band at 480 nm is severely affected by the parasitic contribution by the acceptor C₆₀ to the EQE . In order to approximate the sole contribution of H-type aggregates to the EQE_{max} at 480 nm, these values were conservatively corrected as demonstrated in Figure S9, Supporting Information by deconvolution of each EQE spectrum into the separated contributions of C₆₀ and the donor layer. This must not be performed for the narrow EQE feature at 750 nm of the J-type coupled domains of 1(Hex), as these are optically well isolated from the C₆₀ absorption.

Hence, both EQE_{max} values at 480 and 750 nm of H- and J-coupled domains can be analyzed with respect to the mixing ratio of 1(Pyrl) and 1(Hex) (Figure 2b, **Table 1**; Table S4, Supporting Information). Despite the contribution of C₆₀ and a reduction of the amount of 1(Pyrl) in the mixture, the EQE_{max} of H-type coupled domains remain almost constant up to a mixing ratio

Table 1. Short-circuit current densities (J_{sc}) and external quantum efficiencies at the respective absorption maxima (EQE_{max}) with their bandwidths ($FWHM_{EQE}$) and peak responsivities (R_{max}) of PHJ OPDs with a mixed 1(Pyrl):1(Hex) donor layer at representative mixing ratios in the device architecture ITO/MoO₃/1(Pyrl):1(Hex)/30 nm C₆₀/BCP/Ag. Values for 1(Pyrl) and 1(Hex) were determined at the respective H- and J-type bands at 480 and 754 nm, respectively.

1(Pyrl):1(Hex) ratio	J_{sc} ^{a)} [mA cm ⁻²]	EQE_{max} 1(Pyrl) [%]	EQE_{max} 1(Hex) [%]	$FWHM_{EQE}$ 1(Pyrl) [nm]	$FWHM_{EQE}$ 1(Hex) [nm]	$FWHM_{EQE}$ 1(Pyrl) [cm ⁻¹]	$FWHM_{EQE}$ 1(Hex) [cm ⁻¹]	R_{max} 1(Pyrl) [mA W ⁻¹]	R_{max} 1(Hex) [mA W ⁻¹]
100:0	-2.80 ± 0.01	10 (29) ^{b)}	-	24	-	1040	-	39 (113) ^{b)}	-
50:50	-2.31 ± 0.01	8 (22) ^{b)}	2	24	-	1030	-	33 (86) ^{b)}	9
35:65	-2.27 ± 0.03	7 (20) ^{b)}	7	22	16	940	290	26 (77) ^{b)}	44
25:75	-2.14 ± 0.02	9 (21) ^{b)}	9	15	14	650	240	33 (82) ^{b)}	57
10:90	-1.57 ± 0.01	-	18	-	14	-	250	-	109
0:100	-1.11 ± 0.04	-	14	-	15	-	270	-	85

EQE values were determined at 30 Hz chopping frequency.

^{a)}The given values were determined under AM1.5 G illumination from at least four devices which showed a variation of less than 5%; ^{b)}Values prior to correction for parasitic C₆₀ absorption.

of 20:80, before it strongly decreases with decreasing H-band intensity. Most interestingly, the OPD at a ratio of 10:90 exhibits the highest EQE_{\max} value of 18% at the J-band, exceeding even the 14% with a pristine 1(Hex) donor layer (0:100). To the best of our knowledge this is the to-date highest reported EQE_{\max} value with 18% at 750 nm with a $FWHM$ of only 14 nm for an OPD driven at 0 V sample bias and without photo-multiplication effects based solely on J-aggregation to constitute a narrowband photogeneration feature, exceeding previous literature reported values of 10% at 780 nm ($FWHM = 72$ nm)^[34] and 16% at 756 nm ($FWHM = 125$ nm).^[35] Above a ratio of 50:50 the J-band EQE then vanishes, similar as observed for the thin film in the optical absorption spectra. All $FWHM$ values for the J-band range between 14 and 16 nm ($350\text{--}290$ cm^{-1}) while the $FWHM$ for the H-band are higher with 15–24 nm ($650\text{--}1040$ cm^{-1}). Dually selective OPDs with semitransparent active layers and equal EQE_{\max} at 480 and 752 nm are obtained for mixed layers with mixing ratios of 35:65 (6%) as well as 25:75 (9%) wt%.

From this series of devices with neat and mixed layers of 1(Pyrl) and 1(Hex), the following OPDs stand out for single and dual selectivity: For best H-band selectivity at 480 nm a $FWHM_{EQE}$ of 24 nm (1040 cm^{-1}) and an R of 39 mA W^{-1} were achieved for the neat 1(Pyrl) layer (100:0). Calculations of these OPD figures of merit were done according to established procedures.^[17,18] For the respective J-band of 1(Hex) with best sensitivity at 754 nm a $FWHM_{EQE}$ of 14 nm (250 cm^{-1}) and R of 109 mA W^{-1} were observed at a ratio 10:90. Highest dual selectivity with equal EQE_{\max} values of 9% and respective $FWHM_{EQE}$ of 15 nm (640 cm^{-1}) and 14 nm (240 cm^{-1}) for the H- and J-band at 480 or 754 nm, respectively, were achieved at a 25:75 mixing ratio of both donor materials.

2.4. Charge Transport Properties and Thin Film Morphology

To elucidate the changes in EQE_{\max} with the 1(Pyrl):1(Hex) mixing ratio, the charge transport properties of mixed layers were investigated with OTFTs on Si/SiO₂ substrates at the most relevant mixing ratios. OTFT data (Figure S10, Table S5, Supporting Information) reveal typical p-type characteristics with no significant hysteresis at all mixing ratios. The hole mobility (μ_p) of the mixed donors only varies between 1×10^{-5} and 10×10^{-5} $\text{cm}^2 \text{V}^{-1} \text{s}^{-1}$ for mixing ratios between 100:0 and 25:75, but then significantly increases up to over 3×10^{-3} $\text{cm}^2 \text{V}^{-1} \text{s}^{-1}$ for pristine 1(Hex) layers (0:100). While these findings demonstrate decent charge transport in both neat and mixed layers, they do not completely explain the observed trend in EQE_{\max} values of OPD devices as the lateral conductivity across 100 μm in an OTFT presumably cannot be directly compared to the vertical charge transport across an ≈ 10 nm thick donor layer in an OPD. Thus, the thin film morphology at different mixing ratios was analyzed by atomic force microscopy (AFM) and scanning electron microscopy (SEM), which revealed a large difference in the surface topography at different mixing ratios (Figures S11, Supporting Information). For a neat layer of 1(Pyrl) (100:0) a morphology consisting of polycrystalline rod-like structures with a root-mean-square surface roughness (R_q) of 7.5 nm is measured, which decreases to 4.4 nm at a 75:25 1(Pyrl):1(Hex) mixing ratio. This smoothed and more homogenous surface

structure allows for a more suited interface to the evaporated C₆₀ acceptor layer and thus retains the EQE_{\max} value of 10% of the H-band while the reduced intermixing of the donor and acceptor layers diminishes the contribution of C₆₀ to device performance and thus also the overall J - V -characteristics. At 10:90 a very low R_q of only 1.1 nm compared to the 2.7 nm of the neat 1(Hex) layer (0:100) is observed, both with a similar granular topography. In both cases the C₆₀ contribution to device performance is very low due to a reduced intermixing of the donor and acceptor layers with a simultaneously improved morphology through a reduced grain boundary density compared to higher 1(Pyrl) fractions. This presumably leads to a more favorable contact surface along with the improved charge carrier mobility and thus high EQE_{\max} values for 1(Hex) are obtained. The decreased roughness at a mixing ratio 10:90 therefore leads to an increase in the J-band EQE_{\max} from 14% to 18%, despite a reduced amount of 1(Hex) domains and respective absorption strength in the mixture. Accordingly, next to the absorption strength (OD) of an aggregate's H-/J-band in mixed thin films, the nano-/micro-morphology crucially affects device performance and the resultant EQE_{\max} , as it not only governs the exciton migration length and interface to and contribution of the acceptor but lastly also the charge transport properties and as such requiring well-balanced charge carrier mobility and surface roughness.

2.5. Characterization of Photodiodes with Semitransparent Active Layers

In order to further reduce parasitic absorption by C₆₀ especially at the H-band position and to increase the device transparency and spectral selectivity, the C₆₀ layer thickness was reduced from 30 nm to the lowest limit of 10 nm, which still yielded operational OPDs with sufficient fill factors (FF) of above 45% and 37% for the H- and J-type devices (Figure S12a, Supporting Information), respectively. The higher transparency of these OPDs can be quantified by the transmittance $T\lambda$ via UV-vis-NIR spectroscopy (Figure 3a; Figure S13, Supporting Information), where the main reduction in $T\lambda$ to $\approx 80\%$ in the visible to NIR range can be attributed to the substrate itself and other interlayers. Unfortunately, $T\lambda$ drops to even 70% in the spectral region of C₆₀ (compared to 50% for 30 nm of C₆₀) which gives the layers a yellowish tint. Although the donor materials lead to a further decrease in $T\lambda$ at their respective H- and J-bands down to $< 30\%$, their ultranarrow profiles do not impede the overall color perception of the devices and thus render them very suitable for semitransparent OPDs.

Opto-electronically, these devices retain their ultranarrow bandwidth response with a $FWHM_{EQE}$ of only 21 nm (900 cm^{-1}) and 11 nm (200 cm^{-1}) for the H- and J-bands, respectively (Table 2). The reduced parasitic contribution by C₆₀ to overall current generation can be followed nicely in the R spectra, where both narrowband absorption features are distinctly visible for all three devices with a peak R of 86 mA W^{-1} for the J-Band at 754 nm (Figure 3b). After correction for C₆₀ absorption both the H- and J-band of the single selective devices show similar EQE_{\max} values of 14–15%, while these are respectively reduced to 10% and 5% in the dually selective OPD due to an overall

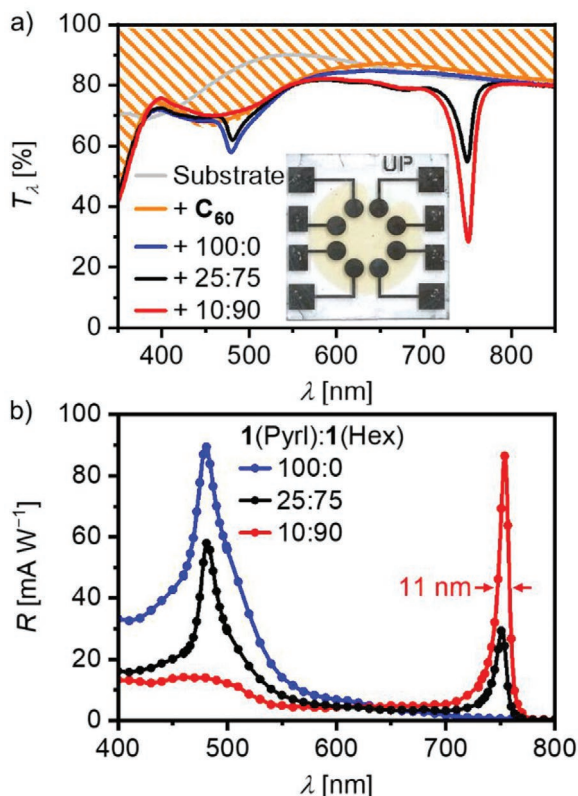


Figure 3. a) UV-vis-NIR transmission (T_λ) spectra of the bare glass/ITO substrate (grey) and of the substrate including all interlayers and 10 nm of C_{60} (orange), and of mixed 1(Pyrl):1(Hex) OPDs in an ITO/MoO₃/1(Pyrl):1(Hex)/10 nm C_{60} /BCP/Ag architecture at mixing ratios of 100:0 (blue), 25:75 (black), and 10:90 (red); the hatched area marks the reduction in T_λ without the donor layers; the inset shows a photograph of the OPD at a mixing ratio of 27:75. b) Spectrally resolved responsivity (R) of all three corresponding OPDs; the solid lines serve as guide to the eye.

lower absorbance at peak positions. All these selective photodetectors show appreciable long-term stability with a reduction of the EQE_{\max} to 98% or 85% of their original values after storage for two weeks under inert conditions (Figure S14, Supporting Information). The resulting specific detectivity (D^*) values for the H- and J-band peak positions of the single selective OPDs equal 3×10^{10} and 2×10^{10} Jones, respectively. These values are calculated from the total measured noise current (Figure S12b, Supporting Information) of the OPDs at a sample bias of 0 V.

Table 2. Photodiode parameters for OPDs in an ITO/MoO₃/1(Pyrl):1(Hex)/10 nm C_{60} /BCP/Ag architecture with 1(Pyrl):1(Hex) mixing ratios of 100:0, 25:75, and 10:90. The metrics for the 25:75 ratio OPD are split into the two LED illumination conditions at 490 and 750 nm, respectively.

1(Pyrl):1(Hex) ratio	V_{oc} [V]	J_{sc} [mA cm ⁻²]	FF [%]	LDR [1 (dB)]	λ_{max} [nm]	EQE_{\max} [%]	$FWHM_{EQE}$ [nm (cm ⁻¹)]	R_{\max} [mA W ⁻¹]	D^*_{\max} [Jones]	f_{-3dB} [kHz]
100:0 @ 490 nm	0.33	2.49	55	10 ⁴ (83)	480	15 (23) ^{a)}	27 (1140)	58 (90) ^{a)}	3×10^{10} (5×10^{10}) ^{a)}	180
25:75 @ 490 nm	0.16	1.30	45	10 ³ (68)	481	10 (15) ^{a)}	21 (900)	40 (58) ^{a)}	1×10^{10} (2×10^{10}) ^{a)}	130
25:75 @ 750 nm	0.11	0.38	37	10 ³ (61)	752	5	12 (210)	29	1×10^{10}	130
10:90 @ 750 nm	0.13	1.23	40	10 ³ (61)	754	14	11 (200)	86	2×10^{10}	150

EQE values were determined at 100 Hz chopping frequency.

^{a)}Values equal data prior to correction for parasitic C_{60} absorption.

Here, the thermal noise component ($7\text{--}14 \times 10^{-13}$ A Hz^{-1/2}) dominates over the shot noise component ($9\text{--}69 \times 10^{-15}$ A Hz^{-1/2}), and as such an overestimation of this key figure of merit is avoided. Under respective single color LED illumination (Figure S15, Supporting Information) the devices show high cut-off frequencies (f_{-3dB} , Figure S12c, Supporting Information) of above 130 kHz, which are estimated to be RC-limited due to respective capacitances and total series resistances of around 10 nF and 100 Ω , respectively,^[20] and demonstrate large linear dynamic ranges (LDR, Figure S12d, Supporting Information) of above 68 and 61 dB for the H- and J-bands, respectively, matching those of commonly used inorganic indium gallium arsenide based photodetectors at 66 dB.^[36]

To demonstrate the application of these devices with semi-transparent active layers, we utilized them in a reflectance-mode PPG sensor. Using this measurement technique, the human heart rate can be conveniently determined non-invasively in dependence on a varying light intensity reflected from the skin surface due to a periodic change in peripheral blood volume (Figure S16a, Supporting Information).^[37] In a simple reflectance mode measurement setup, schematically shown in Figure 4a (Figure S16b, Supporting Information for actual setup), a PPG signal could be collected for all three devices at both band positions using either 490 or 750 nm LED illumination (Figure 4b), allowing for a valid determination of the heart rate to ≈ 58 beats per minute. While the EQE values are lower than for comparable broadband OPD based PPG sensors,^[38] the narrowband response is beneficial as it reduces possible noise through stray light and the OPDs are additionally operated at 0 V sample bias in contrast to a typically used negative bias,^[39] which suits their applicability in low-power consumption wearable devices. While the measurement data presented was collected with a very simple measurement setup, it can nonetheless be observed that the PPG signals at 490 nm appear dampened and less structured due to a considerably lower skin penetration depth. The combination with the selective and more resolved light detection at 750 nm^[40] could enable to measure the blood oxygenation levels within a single device through multi-wavelength detection due to the wavelength-dependent absorption coefficients of hemoglobin in its different oxygenated states.^[38] This demonstrates how multi-wavelength detection is possible with mixed 1(Pyrl):1(Hex) donor layers and that OPDs with such highly transparent active layers exhibit sufficient D^* for biomedical sensing applications.

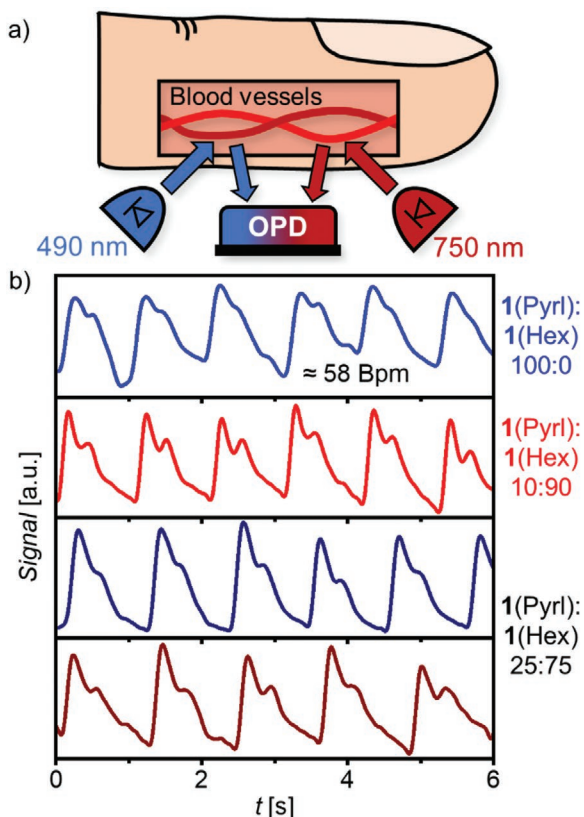


Figure 4. a) Schematic depiction of the measurement setup used for the collection of reflectance-mode PPG signals. b) PPG signals for the best wavelength selective OPDs with mixed **1(Pyrl):1(Hex)** layers at 490 nm LED illumination with mixing ratios of 100:0 (blue) and 25:75 (navy) and at 750 nm illumination with 10:90 (red) and 25:75 (brown).

3. Conclusion

In conclusion, by processing mixed thin films of the two donor materials **1(Pyrl)** and **1(Hex)**, which individually exhibit prominent ultranarrow bandwidth H- and J-type bands in the solid state, respectively, it could be demonstrated that up to 40% of **1(Hex)** molecules can be socially incorporated into the H-type coupled packing arrangement of **1(Pyrl)**. By implementation of < 10 nm thick mixed thin films with well-designed optical and morphological properties into PHJ OPDs, single- and dual-band selective devices were fabricated with full-width at half maxima of down to 11 nm (200 cm^{-1}) and responsivities over 100 mA W^{-1} . Charge transport and morphological investigations showed that the mixing of both dipolar dyes is beneficial for the surface roughness and interface to the C_{60} acceptor, resulting in an increased J-band EQE_{max} value of up to 18%, which exceeds previously reported values for J-aggregates based OPDs driven at 0 V sample bias. By reducing parasitic C_{60} absorption in the OPDs, the spectral selectivity could be further increased in devices with semitransparent active layers, which match inorganic photodiodes in terms of LDR of up to 83 dB and cut-off frequencies of up to 180 kHz. These optimized devices were successfully applied in a PPG bio-medical sensing device.

4. Experimental Section

Synthesis: The synthesis of merocyanine dyes **1(Pyrl)**^[30] and **1(Hex)**^[22] was previously reported. NMR spectroscopy was performed on a Bruker Avance III HD 400 MHz NMR spectrometer relative to residue undeuterated solvent signals. The chemical shifts (δ) are listed in parts per million (ppm).

Preparation of Substrates: As substrates, quartz plates (SUPRASIL, Hellma Analytics) were used for UV-vis-NIR spectroscopy, Si/SiO₂ wafers (SiMat, P/Bor) for OTFT devices, and glass/ITO substrates (Soluxx GmbH, sheet resistance of $15 \Omega \text{ cm}^{-2}$) for OPD devices. Before spin coating, the quartz plates and Si/SiO₂ wafers were successively cleaned with toluene (p.a. grade, VWR chemicals), acetone, and isopropanol (both semiconductor grade VLSI PURANAL, Aldrich Chemistry), followed up by a 30 min UV/ozone treatment. The glass/ITO substrates were cleaned by successive ultrasonication in acetone, Mucosal (1 vol% in deionized water), deionized water and isopropanol, followed by a 30 min UV/ozone treatment, and varnished using a First Contact cleaning solution (Photonic Cleaning Technologies LLC.).

Preparation of Thin Films: Thin films were deposited by spin coating from a CHCl_3 (anhydrous grade, Sigma Aldrich) solution at $4 \times 10^{-3} \text{ M}$ for UV-vis-NIR experiments and 1.5 mg mL^{-1} for device fabrication. For UV-vis-NIR experiments 25 μL of this solution was deposited onto the rotating substrate at 3000 rpm for 30 s. For OTFT and OPD fabrication the solution was spin coated using a static dispense method at 3000 rpm s^{-1} and 3000 rpm for 30 s. Subsequently, all thin films were thermally annealed at $130 \text{ }^\circ\text{C}$ for 5 min on a precision hot plate (PZ28-2, Harry Gestigkeit GmbH).

Characterization in Solid State: Thin film UV-vis-NIR spectra were measured in transmission mode with a PerkinElmer Lambda 950 or Jasco V-770 UV-vis-NIR spectrometer equipped with an integration sphere. Thin-film XRD data were collected on a Bruker D8 Discover diffractometer with a LynxEye-ID-Detector and $\text{Cu}_{K\alpha}$ radiation. SAED measurements were conducted on a FEI Titan 80-300 transmission electron microscope with an accelerating voltage of 150 kV. The thin films for the SAED experiments were prepared by spin coating from a $4 \times 10^{-3} \text{ M}$ CHCl_3 (anhydrous grade, Sigma Aldrich) solution onto PEDOT:PSS coated glass/ITO substrates using a static dispense method (3000 rpm, 3000 rpm s^{-1} , 30 s) with successive annealing at $130 \text{ }^\circ\text{C}$ for 5 min. Afterward, the substrates were immersed in purified water and the floating merocyanine film was taken from the water with carbon-covered copper grids for TEM (Lacey Carbon Films on 200 Mesh Copper Grids, Agar Scientific Ltd.). For the preparation of the substrates, PEDOT:PSS (Heraeus, Clevios P VP Al 4083) was spin coated onto glass/ITO substrates at static dispense (2000 rpm , 4000 rpm s^{-1} , 30 s). AFM was carried out with a Bruker AXS MultiMode 8 scanning probe instrument in tapping mode. Silica cantilevers (OMCL-AC160TS, Olympus) with a spring constant of 26 N m^{-1} and a resonance frequency of $\approx 300 \text{ kHz}$ were used. SEM was carried out with a Zeiss Ultra plus field emission scanning electron microscope equipped with a GEMINI electron beam column operated at 1.5 kV with an aperture size set to 30 μm to avoid excessive charging and radiation damage of the imaged areas.

Fabrication of Organic Thin-Film Transistors: OTFTs were fabricated in a bottom-gate top-contact architecture onto Si/SiO₂ wafers (SiMat, P/Bor). The thin films of merocyanine dyes were fabricated as described above. Afterward, Au electrodes ($W = 200 \mu\text{m}$, $L = 100 \mu\text{m}$) were evaporated in a CreaPhys GmbH OPTIvap-XL system with a rate of $0.1\text{-}2.0 \text{ \AA s}^{-1}$ and a pressure of $< 5 \times 10^{-6} \text{ mbar}$. Prior to characterization, the devices were electrically isolated by removing the surrounding organic material. Then, the devices were characterized under inert conditions (M.Braun Inertgas Systeme GmbH, UNIlab Pro, $c(\text{O}_2) < 1 \text{ ppm}$, $c(\text{H}_2\text{O}) < 1 \text{ ppm}$) by measuring the transfer (saturation regime, $V_{\text{DS}} = -50 \text{ V}$) and output characteristics with an Agilent 4155C parameter analyzer and a Cascade EPS150 probe station.

Fabrication of Organic Photodiodes: OPDs were fabricated in a PHJ ITO/6 nm MoO₃/Merocyanine/30 or 10 nm C₆₀/5 nm BCP/100 nm Ag architecture in a CreaPhys GmbH OPTIvap-XL system. The merocyanine layer was fabricated onto the glass/ITO/MoO₃ substrate as described

in the section preparation of thin films under Experimental Section. Afterward, C₆₀ (CreaPhys GmbH, 2× sublimed) was sublimed with a rate of 0.2 Å s⁻¹ and BCP (Sigma-Aldrich, 99.99%) with a rate of 0.1 Å s⁻¹, both at a pressure of < 2 × 10⁻⁶ mbar, and 100 nm Ag was evaporated with a rate of 2 Å s⁻¹ at a pressure of < 5 × 10⁻⁶ mbar to yield devices with an active area of 7.1 mm².

Device Characterization: Current density versus voltage (*J*-*V*) characteristics under AM 1.5 G white light illumination were measured using a Botest Systems GmbH parameter analyzer with a Newport Oriol Sol3ATM Class AAA solar simulator as a 1000 W m⁻² light source. *J*-*V* characteristics under single color LED illumination at either 490 nm (Thorlabs LED490L) or 750 nm (Thorlabs LED750L) were recorded using an Agilent 4155C parameter analyzer under inert conditions. The LED intensity was calibrated using a Newport 2832-C power meter equipped with a calibrated silicon photodiode (818-SL/DB). The *EQE* was measured using a Newport QE/IPCE Measurement Kit comprised of a 300 W xenon lamp (Newport, 6258), an Oriol Cornerstone monochromator (260 ¼ m, 74125), a Merlin lock-in amplifier (Newport, 70104), an optical chopper operated at a frequency of either 30 or 100 Hz, and a calibrated silicon photodiode (Newport, 70356_70316NS). For measuring transient photoresponse of OPDs, the LED light source was modulated with the built-in function generator of a 70 MHz oscilloscope (Agilent, DSO-X 2002A) using a periodic gate function and signal read-out occurred with the same oscilloscope with a 50 Ω load resistor (Thorlabs, FT500). Up to 10 kHz a 100 kHz electrical lowpass filter (Thorlabs, EF502) was used. Spectral noise density was directly measured by using a signal recovery lock-in amplifier (AMETEK Scientific Instruments, 7265). All above characterization methods were conducted under inert conditions (M. Braun Inertgas Systeme GmbH; *c*(O₂) < 0.1 ppm, *c*(H₂O) < 0.1 ppm). For PPG measurements, the output of the OPDs under LED illumination at ambient conditions was amplified with a low noise pre-amplifier with an A V⁻¹ gain factor of 10⁻⁷ (PerkinElmer instruments, Model 5182) and measured using a 70 MHz oscilloscope with a 100 kHz electrical lowpass filter.

Use of On-Skin Electronics: The PPG measurements using on-skin electronics were performed with the informed consent of all volunteers who participated in the study.

Supporting Information

Supporting Information is available from the Wiley Online Library or from the author.

Acknowledgements

The authors thank the Bavarian Ministry of Education, Science and the Arts for the generous establishment of the Key Laboratory for Supramolecular Polymers of the Bavarian Polymer Institute (BPI) at the Center for Nanosystems Chemistry (CNC) in Würzburg. The skin-attachment experiments displayed in Figure 4 did not require ethics board approval and were performed with the informed consent of all volunteers who participated in the study.

Open access funding enabled and organized by Projekt DEAL.

Conflict of Interest

The authors declare no conflict of interest.

Data Availability Statement

Research data are not shared.

Keywords

exciton coupling, merocyanine dyes/pigments, narrow bandwidth, organic photodiodes, social self-sorting

Received: January 31, 2021

Revised: April 14, 2021

Published online: May 13, 2021

- [1] S.-Y. Chang, P. Cheng, G. Li, Y. Yang, *Joule* **2018**, *2*, 1039.
- [2] P. Müller-Buschbaum, M. Thelakkat, T. F. Fässler, M. Stutzmann, *Adv. Energy Mater.* **2017**, *7*, 1700248.
- [3] E. K. Lee, C. H. Park, J. Lee, H. R. Lee, C. Yang, J. H. Oh, *Adv. Mater.* **2017**, *29*, 1605282.
- [4] C. J. Traverse, R. Pandey, M. C. Barr, R. R. Lunt, *Nat. Energy* **2017**, *2*, 849.
- [5] E. Ravishankar, R. E. Booth, C. Saravitz, H. Sederoff, H. W. Ade, B. T. O' Connor, *Joule* **2020**, *4*, 490.
- [6] H. Khandelwal, A. P. H. J. Schenning, M. G. Debije, *Adv. Energy Mater.* **2017**, *7*, 1602209.
- [7] F. Teng, K. Hu, W. Ouyang, X. Fang, *Adv. Mater.* **2018**, *30*, 1706262.
- [8] F. P. García de Arquer, A. Armin, P. Meredith, E. H. Sargent, *Nat. Rev. Mater.* **2017**, *2*, 16100.
- [9] Y. Guo, C. Liu, H. Tanaka, E. Nakamura, *J. Phys. Chem. Lett.* **2015**, *6*, 535.
- [10] Y. Fang, J. Huang, *Adv. Mater.* **2015**, *27*, 2804.
- [11] J. Song, H. Lee, E. G. Jeong, K. C. Choi, S. Yoo, *Adv. Mater.* **2020**, *32*, 1907539.
- [12] G. Schweicher, G. Garbay, R. Jouclas, F. Vibert, F. Devaux, Y. H. Geerts, *Adv. Mater.* **2020**, *32*, 1905909.
- [13] G. P. Kini, S. J. Jeon, D. K. Moon, *Adv. Mater.* **2020**, *32*, 1906175.
- [14] W. Shi, Y. Guo, Y. Liu, *Adv. Mater.* **2020**, *32*, 1901493.
- [15] P. C. Y. Chow, T. Someya, *Adv. Mater.* **2020**, *32*, 1902045.
- [16] Y. Wang, L. Sun, C. Wang, F. Yang, X. Ren, X. Zhang, H. Dong, W. Hu, *Chem. Soc. Rev.* **2019**, *48*, 1492.
- [17] K.-J. Baeg, M. Binda, D. Natali, M. Caironi, Y.-Y. Noh, *Adv. Mater.* **2013**, *25*, 4267.
- [18] R. D. Jansen-van Vuuren, A. Armin, A. K. Pandey, P. L. Burn, P. Meredith, *Adv. Mater.* **2016**, *28*, 4766.
- [19] V. Pecunia, *J. Phys. Mater.* **2019**, *2*, 042001.
- [20] R. D. Jansen-van Vuuren, A. Pivrikas, A. K. Pandey, P. L. Burn, *J. Mater. Chem. C* **2013**, *1*, 3532.
- [21] S. B. Anantharaman, K. Strassel, M. Diethelm, A. Gubicza, E. Hack, R. Hany, F. A. Nüesch, J. Heier, *J. Mater. Chem. C* **2019**, *7*, 14639.
- [22] A. Liess, A. Arjona-Esteban, A. Kudzus, J. Albert, A.-M. Krause, A. Lv, M. Stolte, K. Meerholz, F. Würthner, *Adv. Funct. Mater.* **2019**, *29*, 1805058.
- [23] A. Armin, R. D. Jansen-van Vuuren, N. Kopidakis, P. L. Burn, P. Meredith, *Nat. Commun.* **2015**, *6*, 6343.
- [24] Y. Zhong, T. J. Sisto, B. Zhang, K. Miyata, X.-Y. Zhu, M. L. Steigerwald, F. Ng, C. Nuckolls, *J. Am. Chem. Soc.* **2017**, *139*, 5644.
- [25] Y. Fang, Q. Dong, Y. Shao, Y. Yuan, J. Huang, *Nat. Photonics* **2015**, *9*, 679.
- [26] B. Siegmund, A. Mischok, J. Benduhn, O. Zeika, S. Ullbrich, F. Nehm, M. Böhm, D. Spoltore, H. Fröb, C. Körner, K. Leo, K. Vandewal, *Nat. Commun.* **2017**, *8*, 15421.
- [27] J. Wang, S. Ullbrich, J.-L. Hou, D. Spoltore, Q. Wang, Z. Ma, Z. Tang, K. Vandewal, *ACS Photonics* **2019**, *6*, 1393.
- [28] F. Elsamnah, A. Bilgaiyan, M. Affiq, C.-H. Shim, H. Ishidai, R. Hattori, *Biosensors* **2019**, *9*, 48.
- [29] Y. Monno, H. Teranaka, K. Yoshizaki, M. Tanaka, M. Okutomi, *IEEE Sens. J.* **2019**, *19*, 497.

- [30] A. Liess, A. Lv, A. Arjona-Esteban, D. Bialas, A.-M. Krause, V. Stepanenko, M. Stolte, F. Würthner, *Nano Lett.* **2017**, *17*, 1719.
- [31] A. Lv, M. Stolte, F. Würthner, *Angew. Chem., Int. Ed.* **2015**, *54*, 10512.
- [32] M. M. Safont-Sempere, G. Fernández, F. Würthner, *Chem. Rev.* **2011**, *111*, 5784.
- [33] S. Ghosh, X.-Q. Li, V. Stepanenko, F. Würthner, *Chem. - Eur. J.* **2008**, *14*, 11343.
- [34] S. B. Anantharaman, K. Strassel, M. Dienthelm, A. Gubicza, E. Hack, R. Hany, F. A. Nüesch, J. Heier, *J. Mater. Chem. C* **2019**, *7*, 14639.
- [35] T. P. Osedach, A. Iacchetti, R. R. Lunt, T. L. Andrew, P. R. Brown, G. M. Akselrod, V. Bulovic, *Appl. Phys. Lett.* **2012**, *101*, 113303.
- [36] X. Gong, M. Tong, Y. Xia, W. Cai, J. S. Moon, Y. Cao, G. Yu, C.-L. Shieh, B. Nilsson, A. J. Heeger, *Science* **2009**, *325*, 1665.
- [37] T. Tamura, *Biomed. Eng. Lett.* **2019**, *9*, 21.
- [38] C. M. Lochner, Y. Khan, A. Pierre, A. C. Arias, *Nat. Commun.* **2014**, *5*, 5745.
- [39] G. Simone, D. Tordera, E. Delvitto, B. Peeters, A. J. J. M. van Breemen, S. C. J. Meskers, R. A. J. Janssen, G. H. Gelinck, *Adv. Optical Mater.* **2020**, *8*, 1901989.
- [40] J. Spigulis, L. Gailite, A. Lihachev, R. Erts, *Appl. Opt.* **2007**, *46*, 10.